

A microwave-activated high-fidelity three-qubit gate scheme for fixed-frequency superconducting qubits

Kui Zhao,¹ Wei-Guo Ma,^{2,3} Ziting Wang,¹ Hao Li,¹ Kaixuan Huang,¹ Yun-Hao Shi,^{2,*} Kai Xu,^{2,1,3,4,†} and Heng Fan^{2,1,3,4,‡}

¹*Beijing Key Laboratory of Fault-Tolerant Quantum Computing, Beijing Academy of Quantum Information Sciences, Beijing 100193, China*

²*Beijing National Laboratory for Condensed Matter Physics, Institute of Physics, Chinese Academy of Sciences, Beijing 100190, China*

³*School of Physical Sciences, University of Chinese Academy of Sciences, Beijing 100049, China*

⁴*Hefei National Laboratory, Hefei 230088, China*

Scalable superconducting quantum processors require balancing critical constraints in coherence, control complexity, and spectral crowding. Fixed-frequency architectures suppress flux noise and simplify control via all-microwave operations but remain limited by residual ZZ crosstalk. Here we propose a microwave-activated three-qubit gate protocol for fixed-frequency transmon qubits in the large-detuning regime ($|\Delta| \gg g$), leveraging the third-order nonlinear interaction to coherently exchange $|001\rangle \leftrightarrow |110\rangle$ states. By incorporating a phase-compensated optimization protocol, numerical simulations demonstrate a high average gate fidelity exceeding 99.9%. Systematic error analysis identifies static long-range ZZ coupling as the dominant error source in multi-qubit systems, which can be suppressed via operations in the large-detuning regime (~ 1 GHz). This approach simultaneously enhances gate fidelity while preserving spectral isolation, ensuring compatibility with existing all-microwave controlled-Z gate frameworks. The protocol exhibits intrinsic robustness to fabrication-induced qubit parameter variations. This hardware-efficient strategy advances scalable quantum computing systems by improving coherence properties, reducing spectral congestion, and expanding the experimental toolkit for error-resilient quantum operations in the noisy intermediate-scale quantum era.

I. INTRODUCTION

Achieving scalable quantum computation requires addressing two concurrent demands: mitigating decoherence in noisy systems and implementing complex algorithms with minimal physical resources. Despite significant progress in quantum error correction [1–4], current quantum technologies still fall short of realizing fault-tolerant universal quantum computation. This limitation becomes particularly critical under the noisy intermediate-scale quantum (NISQ) paradigm [5–7], where full-scale error correction is infeasible, underscoring the need for quantum architectures that support precise two- and multi-qubit operations while maintaining error resilience.

Fixed-frequency superconducting architectures gained prominence as a platform for NISQ devices [8–18], offering enhanced coherence times and simplified control electronics compared to flux-tunable designs [19–31]. These architectures avoid the decoherence channels associated with frequency tuning while enabling all-microwave gate protocols [20, 32]. However, their fixed couplings introduce persistent ZZ crosstalk [13–15], which degrades gate fidelity and restricts operational bandwidth. Conventional approaches such as cross-resonance gates [10–12] further exacerbate these issues by requiring qubit

detunings smaller than their anharmonicities [8, 10, 33], thereby intensifying spectral crowding and imposing stringent fabrication tolerances [34]. Emerging large-detuning architectures help resolve these conflicts by operating in dispersive coupling regimes [35]. These systems effectively suppress static ZZ interactions and enable high-fidelity, microwave-driven controlled-phase (CPhase) and controlled-Z (CZ) gates. This capability not only preserves the intrinsic coherence advantages of fixed-frequency architectures but also enhances their scalability.

However, extending these advances to large-scale multi-qubit operations poses a critical challenge. Three-qubit gates, such as the Toffoli and Fredkin gates, play crucial roles in quantum algorithms [36, 37], quantum simulations [38], and error correction protocols [39–42]. Direct hardware-level implementations of such gates, as opposed to decomposed sequences, offer substantial reductions in circuit depth and enhanced operational flexibility [43]. Recent advances in superconducting quantum circuits have propelled significant progress in implementing three-qubit gates, such as iToffoli [44–46], CCZ [47–53], and iFredkin [16, 54], by leveraging strategies including simultaneous pairwise interactions [55–57], high-level (qutrit, qudit)-assisted protocols [16, 46–48] and coupler (cavity)-assisted architectures [47, 58, 59]. Despite these advancements, practical implementations remain constrained by suboptimal coupling strengths, prolonged high-energy state occupation, and frequency crowding from spurious interactions, which respectively limit gate speeds, amplify decoherence errors, and intro-

* yhshi@iphy.ac.cn

† kaixu@iphy.ac.cn

‡ hfan@iphy.ac.cn

duce fidelity-limiting crosstalk.

In this work, we investigate the implementation of three-qubit gates in large-detuning fixed-frequency architectures. Building on insights from prior studies [60, 61], we propose a microwave-activated gate protocol specifically optimized for large-detuning architectures. The protocol utilizes the intrinsic third-order nonlinearity of transmon qubits to mediate a controlled state exchange ($|001\rangle \leftrightarrow |110\rangle$) using a single microwave drive, enabling selective three-qubit operations. The large-detuning gate scheme is inherently compatible with existing controlled-phase (CPhase) and controlled-Z (CZ) gate protocols [35], allowing seamless integration with standard two-qubit gate frameworks. By combining this protocol with established CZ gate techniques, we demonstrate efficient synthesis of three-qubit gates, such as the iFredkin gate, while retaining the spectral isolation and scalability intrinsic to fixed-frequency architectures. Our work bridges the gap between robust two-qubit operations and high-fidelity multi-qubit control, advancing the toolkit for scalable quantum computing in the NISQ era.

The paper is organized as follows. Section II introduces the superconducting circuit model and establishes the physical mechanism for microwave-activated state-transfer processes, forming the theoretical foundation of the three-qubit gate protocol. Section III systematically explores the dynamics of microwave-driven transitions, elucidating critical relationships between control parameters and coherent population transfer. Section IV quantifies gate performance through numerical simulations, analyzing average fidelity across parameter variations (coupling strengths, detunings) to identify optimal operational regimes. Conclusions and broader implications are summarized in Section V. Appendices provide supplementary technical analyses. Appendix A discusses the origin of the third-order nonlinear interaction for realizing the three-qubit gate. Appendix B details evolution operator simulations, and Appendix C addresses process fidelity evaluation methodologies.

II. SYSTEM AND MODEL

The superconducting circuit system comprises three fixed-frequency transmon qubits with adjacent capacitive couplings, as schematically depicted in Fig. 1(a), governed by the Hamiltonian (hereafter $\hbar = 1$)

$$\hat{H}_0 = \sum_i \left(\omega_i \hat{a}_i^\dagger \hat{a}_i + \frac{\alpha_i}{2} \hat{a}_i^\dagger \hat{a}_i^\dagger \hat{a}_i \hat{a}_i \right) + \sum_{i,j} g_{ij} (\hat{a}_i^\dagger \hat{a}_j + \hat{a}_i \hat{a}_j^\dagger), \quad (1)$$

where ω_i , α_i , and g_{ij} denote qubit frequencies, anharmonicities and pairwise coupling strengths, respectively, for $i, j \in \{A, B, C\}$. The \hat{a}_i (\hat{a}_i^\dagger) denotes the annihilation (creation) operator for q_i . Figure 1(b) shows the energy levels of the total system. The inherent third-order nonlinearity of the transmon qubits allows the microwave drive to modulate the system's Hamiltonian through a

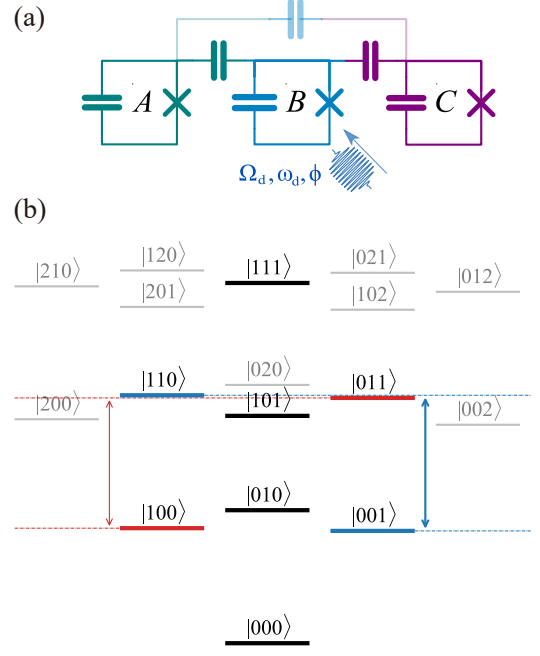


FIG. 1. Circuit diagram and microwave-activated scheme. (a) Circuit schematic of three fixed-frequency transmon qubits (q_A , q_B , q_C) with nearest-neighbor capacitive couplings. The microwave-activated transition is driven by an external microwave field applied to q_B , characterized by amplitude Ω_d and frequency ω_d . (b) Energy-level diagram of the coupled system with a maximum total excitation number below four, where $|n_A n_B n_C\rangle$ denotes the collective state with $n_{A,B,C}$ excitations in each qubit. Within the computational subspace spanned by $\{|000\rangle, |001\rangle, |010\rangle, |011\rangle, |100\rangle, |101\rangle, |110\rangle, |111\rangle\}$. The microwave-activated transition mediates resonant state exchange between $|001\rangle \leftrightarrow |110\rangle$ (blue branch) and $|100\rangle \leftrightarrow |011\rangle$ (red branch), as depicted by the corresponding blue and red double arrows in the energy-level diagram.

four-wave mixing process, facilitating coherent transitions between the distinct states [60–62]. The microwave-activated interaction can be activated by directly driving the central qubit q_B , i.e., $\hat{H}_d = \Omega_d(t) \cos(\omega_d t + \phi) (\hat{a}_B^\dagger + \hat{a}_B)$, where $\Omega_d(t)$ denotes the time-dependent pulse envelope, ω_d represents the drive frequency, and ϕ is the microwave phase. Here we set $\Omega_d(t)$ as the flat-top Gaussian waveform (Fig. 2(a)), parametrized by the maximal amplitude Ω_d , the duration τ and the Gaussian edge σ ($\sigma = 10$ ns, total ramp edge duration 4σ). In the rotating frame, the Hamiltonian can be simplified as

$$\begin{aligned} \hat{H}_{\text{RF}} = & \sum_i \left[(\omega_i - \omega_d) \hat{a}_i^\dagger \hat{a}_i + \frac{\alpha_i}{2} \hat{a}_i^\dagger \hat{a}_i^\dagger \hat{a}_i \hat{a}_i \right] \\ & + \sum_{i,j} g_{ij} (\hat{a}_i^\dagger \hat{a}_j + \hat{a}_i \hat{a}_j^\dagger) + \frac{1}{2} \left[\Omega_d(t) e^{-i\phi} \hat{a}_B^\dagger + \Omega_d^*(t) e^{i\phi} \hat{a}_B \right]. \end{aligned} \quad (2)$$

The above rotating-frame Hamiltonian serves as the foundation for our analysis. In the dispersive regime (where $|g_{A(C)B}/\Delta_{A(C)B}| \ll 1$), the inherent nonlinear-

ity of the qubit enables four-wave mixing processes that coherently couple three qubits with a single drive photon [61, 62]. When the frequency of the external microwave drive precisely matches the energy-level difference between the computational states $|001\rangle \leftrightarrow |110\rangle$ or $|100\rangle \leftrightarrow |011\rangle$ (graphically represented by the red and blue double arrows in Fig. 1(b)), the system mediates microwave-activated effective transitions between these states. The perturbation analysis under the rotating-wave approximation yields an oscillation frequency ν for the $|001\rangle \leftrightarrow |110\rangle$ transition [60]

$$\nu \approx 2 \langle 001 | \hat{H}_{\text{RF}} | 110 \rangle = \frac{2g_{AB}g_{BC}\alpha_B\Omega_d}{\Delta_{AC}\Delta_{BC}(\Delta_{BA} + \alpha_B)}, \quad (3)$$

where $\Delta_{ij} = \omega_i - \omega_j$. Without loss of generality, we adopt the convention $\omega_A > \omega_C$ throughout the following analysis.

Note that the microwave-activated transitions enable controlled state exchange between $|001\rangle \leftrightarrow |110\rangle$ (blue branch) and $|100\rangle \leftrightarrow |011\rangle$ (red branch), distinguished by their unique transition frequencies. The red branch operates at a frequency below ω_B , making it susceptible to off-resonant effects such as single-photon ($|101\rangle \leftrightarrow |210\rangle$) and two-photon ($|000\rangle \leftrightarrow |020\rangle$, $|001\rangle \leftrightarrow |120\rangle$) transitions [60]. In contrast, the blue branch operates at a frequency above ω_B , which suppresses spurious transitions on the high-frequency side of ω_B due to the negative anharmonicity of the transmon. This intrinsic spectral isolation establishes the blue branch as the superior platform for implementing high-fidelity gates. Based on the foundational work of Shotaro [60] on microwave-driven CZ gates via cyclic transitions in qubit-coupler-qubit architectures, we demonstrate a high-fidelity three-qubit gate protocol utilizing the microwave-activated $|001\rangle \leftrightarrow |110\rangle$ state exchange. This approach retains the inherent advantages of fixed-frequency architectures, such as minimized frequency crowding and robust coherence, while expanding their functional versatility for multi-qubit operations.

III. MICROWAVE-ACTIVATED TRANSITION

In this section, we investigate the dynamics of microwave-activated transitions in a three-transmon circuit through numerical simulations. The simulations, implemented using QuTiP [63], model a capacitively coupled fixed-frequency transmon system governed by the Hamiltonian in Eq. (2). Each qubit is truncated at the fourth excited state to balance computational efficiency with physical accuracy, capturing essential nonlinear behavior while maintaining numerical stability. The parameters are designed to align with experimental implementations [60] while strategically enhancing the detuning between nearest-neighbor (NN) qubits, with the corresponding frequencies $\omega_{A,B,C}/2\pi = \{5.641, 6.517, 5.507\}$ GHz, anharmonicities $\alpha_{A,B,C}/2\pi = \{-300, -381, -303\}$ MHz, NN cou-

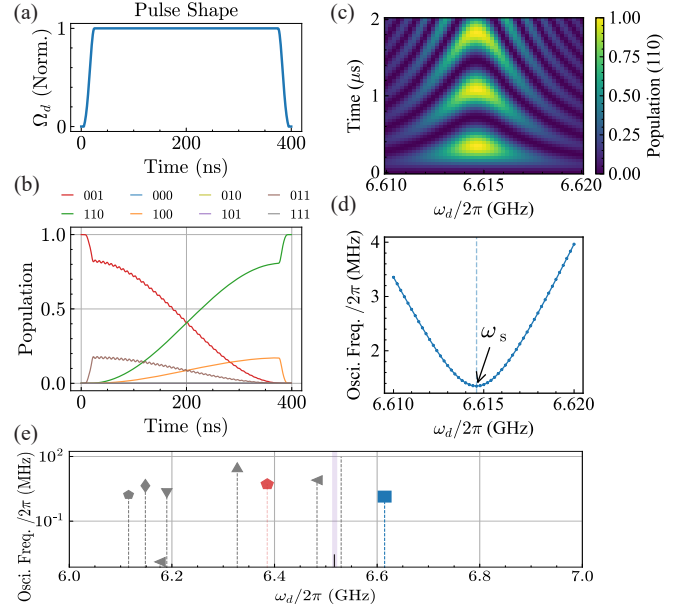


FIG. 2. Pulse shape profile and microwave-activated state-transfer dynamics. (a) Numerically simulated pulse envelope (blue trace) featuring a flat-top profile with Gaussian edges ($\sigma = 10$ ns, total edge duration 4σ). (b) microwave-activated resonant state exchange between $|001\rangle$ and $|110\rangle$, achieving $> 99.9\%$ population transfer fidelity from the initial $|001\rangle$ state. Notably, all non-target computational states remain unpopulated ($< 0.1\%$), highlighting intrinsic state selectivity of the protocol. (c) Population of the $|110\rangle$ state for the microwave-activated transition as a function of drive frequency ω_d and duration time, obtained by a numerical simulation of the transmon Hamiltonian (Eq. (2)) when the system is initialized in $|001\rangle$ state. (d) Extracted oscillation frequencies from (c) align with the theoretical value of approximately 1.25 MHz. (e) Broadband spectroscopy. The spectrum reveals spectral features, including a primary blue branch resonance (blue), a red branch sideband (red), sidebands around ω_B and distant features.

pling strengths $g_{AB}/2\pi = 40$ MHz and $g_{BC}/2\pi = 31$ MHz, and a next-nearest-neighbor (NNN) coupling $g_{AC}/2\pi = 1.9$ MHz. The above parameter configuration preserves the intrinsic scalability of fixed-frequency architectures while maintaining compatibility with established high-fidelity CPhase gate protocols [35].

Despite operating in a large-detuning regime, the fixed capacitive couplings inherently introduce static ZZ interactions, with NN ZZ couplings calculated as $\xi_{AB}/2\pi \approx -3.7$ MHz and $\xi_{BC}/2\pi \approx -1.5$ MHz, in agreement with perturbation formula [21]

$$\xi_{ij} = \frac{2g_{ij}^2(\alpha_i + \alpha_j)}{(\Delta_{ij} + \alpha_i)(\Delta_{ij} - \alpha_j)}. \quad (4)$$

Note that the large detuning (~ 1.0 GHz) between NN qubits yields $\xi_{AC}/2\pi \approx 6.9$ kHz, which implies that the long-range ZZ interaction can be significantly suppressed. Although static ZZ couplings may introduce parasitic CPhase phase errors (see subsequent numerical analyses),

recent advances in fixed-coupling architectures demonstrate that simultaneous off-resonant Stark tones can further suppress these residual interactions [14, 15], offering a complementary strategy for error mitigation.

To probe the dynamics of the microwave-activated transition, we apply a flat-top Gaussian-edged pulse ($\sigma = 10$ ns, total edge duration $= 4\sigma$) to qubit q_B . The pulse profile is illustrated in Fig. 2(a). When driving at the transition frequency ($\omega_d = \omega_s$), the protocol achieves coherent states exchange between $|001\rangle$ and $|110\rangle$, as shown in Fig. 2(b). Meanwhile, all non-target computational states maintain negligible population, confirming the state selectivity of our protocol and validating the state-transfer due to the microwave-activated transition. To further characterize the microwave-activated protocol, we initialize the system in $|001\rangle$ and vary the drive frequency (ω_d) and pulse duration. Figure 2(c) illustrates the resulting the population of $|110\rangle$ near the predicted resonance $\omega_s \sim \omega_B + \Delta_{AC}$, revealing a pronounced population transfer. The corresponding oscillation frequencies extracted from time-domain, as shown in Fig. 2(d), exhibit excellent agreement with the predicted value of approximately 1.25 MHz obtained from Eq. (3). To further quantify the off-resonant transitions near ω_s , Figure 2(c) shows the oscillation frequencies of the $|001\rangle$ population across a wide drive-frequency range, initialized from $|001\rangle$. The spectrum exhibits a primary blue branch resonance (blue point), a red branch sideband (red point), sidebands near ω_B from higher-order nonlinear transitions, with negligible distant features. Notably, the spectral sparsity around the target ω_s , inherent to the large-detuning regime ($\omega_B \gg \omega_A, \omega_C$), suppresses parasitic couplings and ensures strong isolation from the nearest sidebands.

IV. MICROWAVE-ACTIVATED THREE-QUBIT GATE PERFORMANCE

The microwave-activated state-transfer mechanism enables coherent population exchange between states $|001\rangle$ and $|110\rangle$ in a three-qubit system, providing the foundation for an three-qubit gate. During this process, the target states acquire a characteristic $-i$ phase factor while all other computational states remain unaffected. However, the drive pulse inevitably induces off-resonant transitions that dynamically perturb neighboring states, leading to unintended phase shifts. Additionally, static ZZ couplings inherent to fixed-frequency architectures cause conditional phase accumulations, further distorting the ideal unitary operation. To mitigate these undesired effects, we implement a targeted phase correction protocol using the unitary U_{phase} , combining CPhase terms and single-qubit Z-rotations, as illustrated in Fig. 3(a). The CPhase operation is defined by the diagonal matrix, $U_{\text{CPhase}} = \text{diag}[1, 1, 1, e^{-i\theta_{BC}}, 1, 1, e^{-i\theta_{AB}}, e^{-i(\theta_{AB}+\theta_{BC})}]$, where $\theta_{jk} = \xi_{jk}t$ encodes the ZZ-mediated phase accumulation

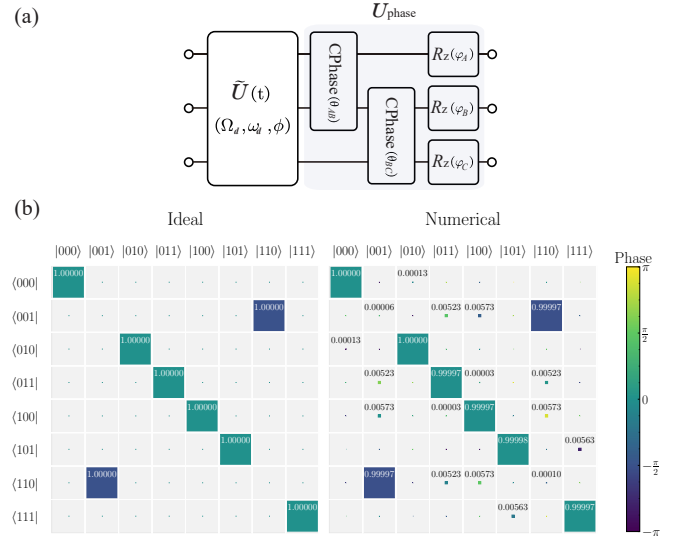


FIG. 3. Phase correction protocol and truth table. (a) Schematic of the phase correction protocol, integrating the microwave-activated unitary $\tilde{U}(\Omega_d, \omega_d, \phi)$ and the correction unitary U_{phase} . In $\tilde{U}(\Omega_d, \omega_d, \phi)$, ϕ represents the dynamically optimized pulse phase designed to suppress transient phase errors. The correction unitary U_{phase} , applied after the microwave-activated operation, consists of two CPhase terms (θ_{AB}, θ_{BC}) for qubit pairs AB and BC , as well as three single-qubit virtual Z-rotations ($\varphi_A, \varphi_B, \varphi_C$). By optimizing these six parameters ($\theta_{AB}, \theta_{BC}, \varphi_A, \varphi_B, \varphi_C, \phi$), the protocol achieves high-fidelity three-qubit gates with minimized static and dynamic phase errors. (b) Truth table at $\Omega_d/2\pi \approx 90$ MHz, comparing the ideal gate unitary (left) with numerical simulation results (right). The protocol achieves an average fidelity of 99.9% and demonstrates near-perfect population transfer.

between NN qubits q_j and q_k , while single-qubit phases ($\varphi_A, \varphi_B, \varphi_C$) are applied as virtual corrections. Additionally, the microwave pulse phase ϕ is also considered to ensure full cancellation of both dynamic and static phase errors. This hierarchical compensation scheme addresses dominant CPhase errors between NN qubits through tailored corrections while adhering to hardware constraints that restrict high-fidelity CPhase operations to directly coupled pairs. Residual errors from NNN ZZ coupling (e.g., $\xi_{AC} \approx 10$ kHz) are passively suppressed by the intrinsic dispersive regime, eliminating the need for additional error suppression. By canceling both static and dynamically induced phase errors without compromising experimental simplicity, the protocol can achieve robust gate performance in scalable fixed-frequency qubit systems.

By applying U_{phase} to the microwave-activated unitary \tilde{U} , the desired three-qubit gate unitary U' can be expressed as

$$U' = U_{\text{phase}} \tilde{U}. \quad (5)$$

The corresponding ideal matrix in the computational ba-

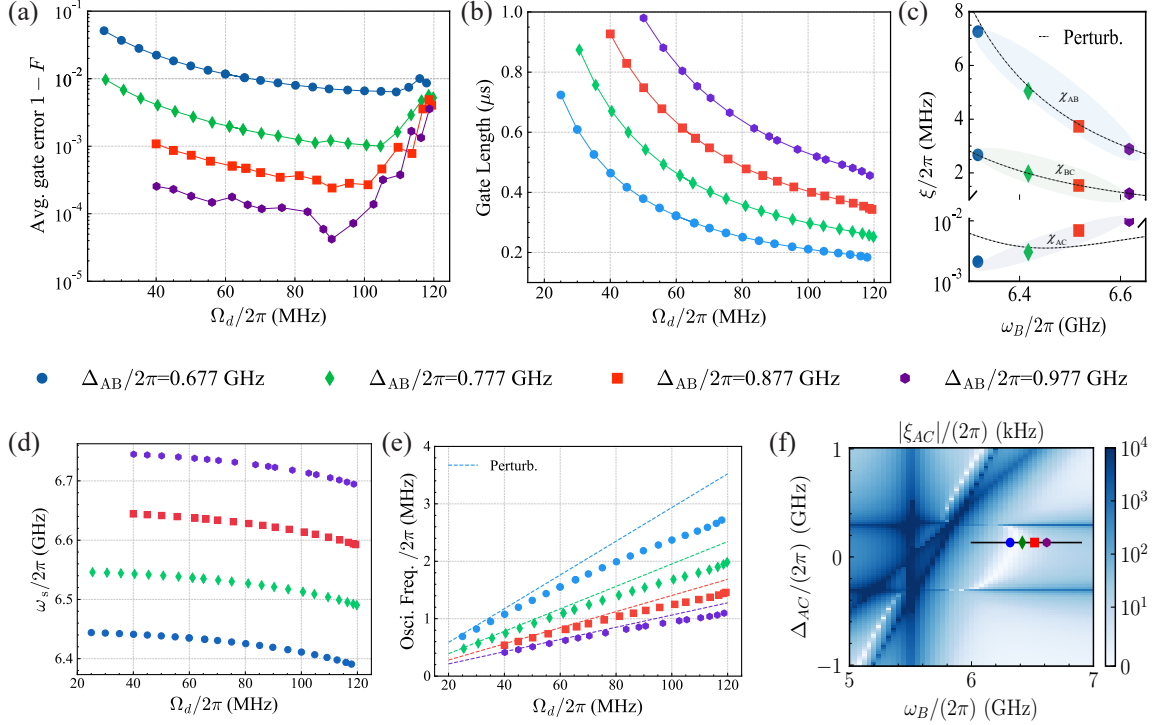


FIG. 4. Gate error versus drive amplitude and qubit detuning. (a) Average gate error $1 - F$ as a function of drive amplitude Ω_d for varying NN detunings $\Delta_{AB}/2\pi = \{0.677, 0.777, 0.877, 0.977\}$ GHz (blue, green, red, purple curves). Increasing Δ_{AB} reduces errors from $\sim 10^{-2}$ to $\sim 10^{-4}$, demonstrating the advantage of large detuning. (b) Gate duration decreases with increasing drive amplitude ω_d and decreasing Δ_{AB} , reflecting the inverse proportionality between oscillation frequency ν and Δ_{AB} (Eq. (3)). (c) Static ZZ couplings ξ_{AB} and ξ_{BC} increase with reduced ω_B , while the NNN coupling ξ_{AC} remains suppressed below 10 kHz due to the large detuning. Dashed lines correspond to fourth-order perturbative calculations of static ZZ couplings. (d) Transition frequency ω_{tran} as a function of Ω_d , showing systematic shifts under varying drive amplitudes and detunings. (e) Numerical results for ν (points) compared to perturbative predictions (solid line, Eq. (3)) at high Ω_d , particularly for small detunings, highlighting the need for beyond-perturbative modeling in strongly driven regimes. (f) $|\xi_{AC}|/(2\pi)$ versus ω_B and ω_A (fixed $\omega_C/2\pi = 5.507$ GHz). Black solid-line traces highlight four selected NN detuning configurations, corresponding to $\Delta_{AB}/2\pi = \{0.677, 0.777, 0.877, 0.977\}$ GHz, concentrated within near-zero ξ_{AC} regions, revealing strong long-range ZZ suppression in the large-detuning regime.

sis is

$$U_i = \begin{pmatrix} 1 & 0 & 0 & 0 & 0 & 0 & 0 & 0 \\ 0 & 0 & 0 & 0 & 0 & 0 & -i & 0 \\ 0 & 0 & 1 & 0 & 0 & 0 & 0 & 0 \\ 0 & 0 & 0 & 1 & 0 & 0 & 0 & 0 \\ 0 & 0 & 0 & 0 & 1 & 0 & 0 & 0 \\ 0 & 0 & 0 & 0 & 0 & 1 & 0 & 0 \\ 0 & -i & 0 & 0 & 0 & 0 & 0 & 0 \\ 0 & 0 & 0 & 0 & 0 & 0 & 0 & 1 \end{pmatrix}, \quad (6)$$

which induces the $|001\rangle \leftrightarrow |110\rangle$ exchange with $-i$ phase, analogous to an iSWAP operation scaled to three qubits. This operation ensures that only the targeted states undergo the desired phase transformation, while all other computational states remain unaffected.

To determine the optimal operating parameters for a three-qubit gate, the numerical optimization proceeds through four key stages. The process begins by conducting 2D Rabi spectroscopy at a fixed driving strength Ω_d to accurately determine the dressed transition frequency

ω_s . Based on this, we perform numerical simulations of the system dynamics to identify the minimal gate duration required to enable a complete $|001\rangle \leftrightarrow |110\rangle$ state exchange. We then optimize the gate parameters by performing a local search in the neighborhood of the initial parameter space to maximize state-transfer population. This optimization incorporates the quadrature term (derivative removal via adiabatic gate, DRAG) for pulse edges to suppress leakage errors [64–67]. Based on this, the microwave-activated unitary operation \tilde{U} is subsequently obtained from numerical simulations of the dynamical evolution governed by Eq. (2). After applying phase compensation to eliminate phase distortions, we construct the phase corrected unitary U' using Eq. (5). The average gate fidelity is evaluated using the standard metric [59, 68, 69],

$$F = \frac{|\text{Tr}(U_{\text{ideal}}^\dagger U')|^2 + \text{Tr}(U'^\dagger U')}{d(d+1)}, \quad (7)$$

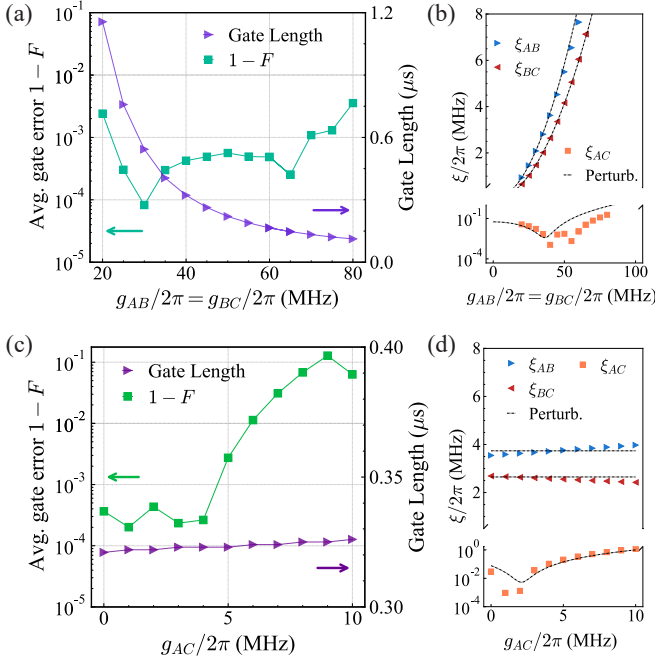


FIG. 5. Gate error dependence on qubit coupling parameters. (a) Gate error (cyan curve, left axis) and gate duration (purple curve, right axis) as functions of the NN coupling strengths $g_{AB}/2\pi = g_{BC}/2\pi$, under a fixed microwave drive amplitude $\Omega_d = 100$ MHz. The gate error remains below 10^{-3} across a broad NN coupling range of 40–60 MHz, demonstrating robust performance. Gate durations exhibit an inverse proportionality to coupling strength, while gate durations inversely scale with coupling strength, requiring longer operation times for weaker couplings. (b) Static ZZ couplings ($\xi_{AB}, \xi_{BC}, \xi_{AC}$) as functions of $g_{AB}/2\pi = g_{BC}/2\pi$, with dashed curves showing perturbative predictions. (c) Gate error (green curve) and duration (purple curve) versus NNN coupling $g_{AC}/2\pi$ under fixed $g_{AB}/2\pi = g_{BC}/2\pi = 40$ MHz and $\Omega_d = 100$ MHz. Error suppression below 10^{-3} persists for $g_{AC}/2\pi \leq 4$ MHz but degrades with stronger couplings. (d) Static ZZ couplings ($\xi_{AB}, \xi_{BC}, \xi_{AC}$) as functions of $g_{AC}/2\pi = g_{BC}/2\pi$, with dashed curves showing perturbative predictions. Growth of NNN static ZZ coupling ξ_{AC} as a function of $g_{AC}/2\pi$, correlating with the fidelity degradation observed in (c).

where $d = 8$ represents the total dimension for the three-qubit system and U_{ideal} denotes the ideal gate defined in Eq. (6).

Following the targeted phase correction protocol applied to the derived evolution operator, we achieve an average gate fidelity exceeding $\geq 99.9\%$ under parameters ($\Omega_d/2\pi \approx 90$ MHz, gate duration ≈ 400 ns). Figure 3(b) compares the ideal truth table of the target operation U_{ideal} (left panel) with the numerically corrected unitary U' (right panel). The comparison demonstrates consistent population transfer across all computational states and strong agreement between the theoretical gate operation and simulated outcomes.

Next, we investigate the gate performance under varying qubit parameters by exploring its depen-

dence on NN detunings. We fix the frequencies of qubits q_A and q_C at 5.641 GHz and 5.507 GHz, while varying the frequency of q_B across $\omega_B/2\pi = \{6.317, 6.417, 6.517, 6.617\}$ GHz. This corresponds to NN detunings $\Delta_{AB}/2\pi = \{0.677, 0.777, 0.877, 0.977\}$ GHz. Numerical simulations under these conditions are summarized in Fig. 4. Figure 4(a) shows the average gate error $1 - F$ as a function of drive amplitude Ω_d for different Δ_{AB} . The blue, green, red, and purple curves correspond to $\Delta_{AB}/2\pi = \{0.677, 0.777, 0.877, 0.977\}$ GHz, respectively. Notably, increasing Δ_{AB} enhances gate fidelity, with gate errors decreasing from around 10^{-2} at $\Delta_{AB} = 0.677$ GHz to around 10^{-4} at $\Delta_{AB} = 0.977$ GHz. This improvement highlights the advantage of operating in the large-detuning regime. Figures 4(b)-(e) present the numerical results for gate duration, transition frequency ω_{tran} , and oscillation frequency ν as functions of Ω_d . As shown in Fig. 4(b), the gate duration decreases with higher drive amplitudes and smaller NN detunings, reflecting the inverse proportionality between ν and Δ_{AB} , predicted by Eq. (3). This relationship is further corroborated in Fig. 4(e), where the solid line represents the perturbative results from Eq. (3). Deviations from perturbation theory emerge at larger drive amplitudes, particularly for smaller Δ_{AB} , indicating the restricted validity of the perturbative approximation under strong driving. The static ZZ coupling characteristics are systematically investigated in Fig. 4(c). While NN static ZZ couplings (ξ_{AB}, ξ_{BC}) grow with decreasing detuning Δ_{AB} , the NNN coupling ξ_{AC} remains suppressed below 10 kHz, demonstrating the protective effect of large NN detunings. The dashed curves confirm agreement with perturbative calculations, where NN ZZ couplings follow the analytical expression in Eq. (4), while the NNN coupling is derived from fourth-order perturbation theory, as detailed in Refs. [26, 70]. Figure 4(f) shows the NNN ZZ coupling ξ_{AC} as a function of ω_B and Δ_{AC} , with the colored points along black solid line marks four configurations of the selected NN detunings $\Delta_{AB}/2\pi = \{0.677, 0.777, 0.877, 0.977\}$ GHz. These configurations consistently reside in parameter regimes where ξ_{AC} approaches zero, reflecting the inherent long-range ZZ suppression enabled by the large-detuning regime.

We further investigate the gate performance under varying qubit parameters, including NN coupling strengths g_{AB}, g_{BC} and NNN coupling g_{AC} , with ω_B fixed at 6.517 GHz. Figure 5(a) shows the gate error (cyan curve) as a function of $g_{AB} = g_{BC}$ under a fixed drive amplitude $\Omega_d = 100$ MHz. Notably, the gate achieves sub- 10^{-3} errors across a broad NN coupling range of [40, 60] MHz. The corresponding gate durations (purple curve) exhibit an inverse relationship with coupling strength, where weaker NN couplings necessitate longer gate times. The static ZZ coupling are analyzed in Fig. 5(b). Reducing NN coupling strengths suppresses the NN static ZZ couplings (ξ_{AB}, ξ_{BC}), while stronger NN couplings amplify the NNN coupling ξ_{AC} , leading to long-range crosstalks and phase errors. We further explore

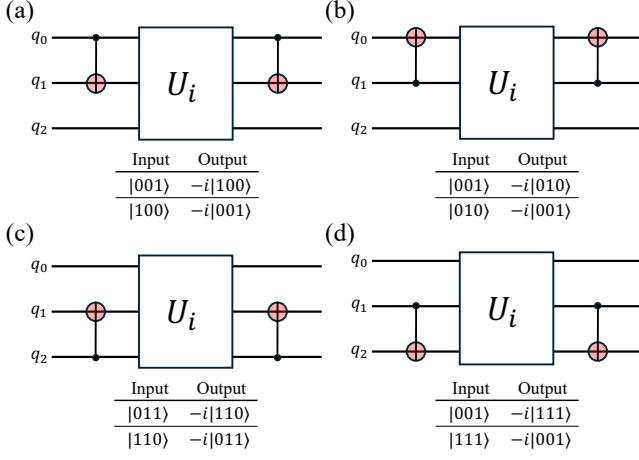


FIG. 6. Implementation of iFredkin (controlled-SWAP) gate through combining U_i and CNOT operations. (a) $|0\rangle$ -control on q_2 : swaps q_1 and q_3 ($|001\rangle \leftrightarrow |110\rangle$) with $-i$ phase. (b) $|0\rangle$ -control on q_1 : swaps q_2 and q_3 ($|001\rangle \leftrightarrow |010\rangle$). (c) $|1\rangle$ -control on q_2 : swaps q_2 and q_3 ($|011\rangle \leftrightarrow |110\rangle$). (d) $|1\rangle$ -control on q_3 : global flip when $q_1 = q_2$ ($|001\rangle \leftrightarrow |111\rangle$). Each configuration selectively swaps qubit pairs under distinct control conditions while preserving non-target states.

the gate performance under varying NNN coupling g_{AC} with $g_{AB}/2\pi = g_{BC}/2\pi = 40$ MHz and $\Omega_d = 100$ MHz, as shown in Fig. 5(c). We further investigate the influence of NNN coupling g_{AC} on gate performance under fixed parameters $g_{AB}/2\pi = g_{BC}/2\pi = 40$ MHz and drive amplitude $\Omega_d = 100$ MHz. As shown in Fig. 5(c), the gate error remains below 10^{-3} for $g_{AC}/2\pi \in [0, 4]$ MHz, but increases as g_{AC} exceeds this range. This degradation correlates with the rise of static ZZ coupling ξ_{AC} , as demonstrated by its growth with g_{AC} in Fig. 5(d). Notably, we observe a pronounced correlation between gate error and the NNN static ZZ coupling ξ_{AC} . The underlying mechanism stems from the persistent static ZZ coupling in fixed-coupling architectures, which introduces undesired CPhase errors. While NN ZZ couplings (ξ_{AB} and ξ_{BC}) have been actively compensated through phase compensation protocols, the NNN static ZZ coupling ξ_{AC} induces uncompensated phase errors. These residual errors accumulate during gate operations, ultimately limiting the gate fidelity as g_{AC} increases.

These results highlight the resilience of the protocol to fabrication variations, which is a vital feature for scalable superconducting quantum systems. The observed parameter tolerance stems from the interplay between drive-activated nonlinearity and dispersive protection, enabling robust gate operation even with $\pm 5\%$ deviations in qubit frequencies or couplings. This adaptability positions the gate framework as a practical solution for high-fidelity multi-qubit operations in real-world quantum processors.

The microwave-activated three-qubit gate proposed here can be used to directly constructing universal iFred-

kin (controlled-SWAP) gates. These gates share a common operational framework as members of the controlled-SWAP family, where the iFredkin gate requires only two additional controlled-NOT (CNOT) gate operations to transform the base unitary. Figure 6 demonstrates the direct construction of an iFredkin gate using the microwave-activated three-qubit gate. Specifically, applying CNOT gates on NN qubits enables different iFredkin gate configurations, as shown in Fig. 6. Crucially, our protocol remains fully compatible with the existing large-detuning fixed-frequency architectures that utilize microwave-activated CZ gates [35]. In such systems, each CNOT gate is implemented via an all-microwave CZ gate and a single qubit gate, ensuring the integration of the iFredkin gate without hardware modifications.

V. CONCLUSION

In summary, we demonstrate a microwave-activated three-qubit gate scheme designed for large-detuning fixed-frequency transmon architectures, offering a practical approach to extend the operational capabilities of superconducting quantum processors. By virtue of the intrinsic third-order nonlinearity of transmon qubits under large-detuning conditions ($|\Delta| \gg g$), we implement a three-qubit operation that coherently exchanges $|001\rangle \leftrightarrow |110\rangle$ states via a single microwave drive. Numerical simulations confirm 99.9% average gate fidelity under large-detuning conditions, achieving simultaneous spectral isolation to suppress ZZ crosstalk and mitigate frequency crowding. The compatibility of architecture with existing CZ and CPhase gate frameworks ensures seamless integration into current fixed-frequency quantum platforms, preserving their inherent coherence advantages and hardware efficiency.

The proposed three-qubit gate scheme addresses two key limitations in multi-qubit gate design: it eliminates the need for auxiliary couplers or qutrit transitions, thereby avoiding decoherence pathways associated with high-energy states, and leverages detuning-dominated operation to enhance robustness against parameter variations. By operating in the dispersive coupling regime, the protocol not only suppresses unwanted interactions but also simplifies control requirements through all-microwave driving. This enables direct implement of three-qubit gates without decomposing them into elementary single- and two-qubit operations, which reduces circuit depth and enhances algorithmic flexibility for near-term quantum applications. Our results reinforce the potential of fixed-frequency superconducting platforms as a viable substrate for advancing scalable quantum computation, bridging the gap between robust two-qubit operations and the demands of multi-qubit control.

ACKNOWLEDGMENTS

This work was supported by National Natural Science Foundation of China (Grants Nos. 92265207, T2121001, 12122504, T2322030, 92365301), the Innovation Program for Quantum Science and Technology (Grant No. 2021ZD0301800), Beijing Nova Program (Nos. 20220484121, 2022000216), Beijing National Laboratory for Condensed Matter Physics (2024BNL-CMPKF022), and the China Postdoctoral Science Foundation (Grant No. GZB20240815).

Appendix A: The Effective Hamiltonian

In this section, we briefly discuss the physical origin of four-wave mixing (4WM) in our system. This phenomenon arises primarily from the inherent nonlinearity of the central qubit q_B , consistent with mechanisms reported in Refs. [61, 62, 71]. To clarify, we approximate the system as three linear photonic modes coupled via the Josephson junction of q_B , governed by the Hamiltonian

$$\hat{H} = \sum_j \omega_j \hat{a}_j^\dagger \hat{a}_j - E_J \left[\cos \hat{\varphi} + \frac{\hat{\varphi}^2}{2} \right] + \Omega_d \cos(\omega_d t) (\hat{a}_B^\dagger + \hat{a}_B), \quad (\text{A1})$$

where $j \in \{A, B, C\}$ and $\hat{\varphi} = \sum_j \varphi_j (\hat{a}_j + \hat{a}_j^\dagger)$ represents the phase across the junction. The cosine term encodes the Josephson nonlinearity, with E_J denoting the Josephson energy.

In the regime $\omega_j \gg \Omega_d$, one can use the rotating frame to eliminate high-frequency items and obtain the effective Hamiltonian

$$\hat{H}' = \sum_{j \in \{A, B, C\}} \delta_j \hat{a}_j^\dagger \hat{a}_j - E_J \left(\cos \hat{\varphi}' + \frac{\hat{\varphi}'^2}{2} \right), \quad (\text{A2})$$

with

$$\begin{aligned} \hat{\varphi}' &= \varphi_B (\xi_d e^{-i\omega_d t} + \xi_d^* e^{i\omega_d t}) \\ &+ \sum_{j \in \{A, B, C\}} \varphi_j \left[\hat{a}_j e^{-i(\omega_j - \delta_j)t} + \hat{a}_j^\dagger e^{i(\omega_j - \delta_j)t} \right], \end{aligned} \quad (\text{A3})$$

where $\omega_d = (\omega_B - \delta_B) + (\omega_A - \delta_A) - (\omega_C - \delta_C)$, $\delta_{A,B,C}$ are arbitrary detunings, and the drive mode is approximated by its mean-field amplitude $\xi_d e^{-i\omega_d t}$, $\xi_d = \Omega_d/(\omega_d - \omega_B)$ [62], reflecting the drive-induced displacement. By expanding the cosine term to fourth order and retaining non-rotating terms, we obtain the effective Hamiltonian

$$\hat{H}' \approx \hat{H}_{\text{Stark}} + \hat{H}_{\text{Kerr}} + \hat{H}_{4\text{WM}}, \quad (\text{A4})$$

which includes three dominant contributions: Stark shifts, Kerr nonlinearities, and four-wave mixing. The Stark shift term modifies mode frequencies, i.e.,

$$\hat{H}_{\text{Stark}} = \left(\delta_B - 2\chi_{BB} |\xi_d|^2 \right) \hat{a}_B^\dagger \hat{a}_B + \sum_{j \in \{A, C\}} (\delta_j - \chi_{Bj} |\xi_d|^2) \hat{a}_j^\dagger \hat{a}_j, \quad (\text{A5})$$

while Kerr nonlinearities introduce anharmonicity via term

$$\hat{H}_{\text{Kerr}} = - \sum_{j=A,B,C} \chi_{jj} \hat{a}_j^{\dagger 2} \hat{a}_j^2 - \sum_{k,l} \chi_{kl} \hat{a}_k^\dagger \hat{a}_k \hat{a}_l^\dagger \hat{a}_l, \quad (\text{A6})$$

with coefficient $\chi_{kl} = E_J \phi_k^2 \phi_l^2$ and $kl \in \{AB, BC, AC\}$. The critical 4WM term emerges as

$$\hat{H}_{4\text{WM}} = g_3 \hat{a}_A^\dagger \hat{a}_B^\dagger \hat{a}_C + \text{H.c.}, \quad (\text{A7})$$

and the third-order nonlinear coupling g_3 is given by

$$g_3 = -\xi_d \sqrt{\chi_{AB} \chi_{BC}}, \quad (\text{A8})$$

where χ_{AB} corresponds to the dispersive shift of qubit B , and it can be approximated as

$$\chi_{AB} \approx \frac{1}{1 + \Delta_{AB}/\alpha_B} \left(\frac{g_{AB}}{\Delta_{AB}} \right)^2. \quad (\text{A9})$$

The analytical expression derived here exhibits significantly improved agreement with experimental data compared to the perturbative approach outlined in Eq. (3), as quantitatively demonstrated in Fig. 7. The 4WM process originates from the qubit-mediated nonlinear interaction among qubit modes where the drive photon parametrically activates the resonant coupling condition

$$\omega_d = \omega_B + \omega_C - \omega_A - \chi_{BC} - |\xi_d|^2 (2\chi_{BB} + \chi_{BC} - \chi_{AB}), \quad (\text{A10})$$

where $\chi_{BB} = \alpha_B$. The above parametric resonance drives coherent population transfer between $|001\rangle$ and $|110\rangle$. A comprehensive perturbative analysis of this process can be found in Ref. [60]. Such controlled nonlinear coupling forms the foundation of the microwave-activated three-qubit gate, directly linking the drive amplitude to the tunable 4WM strength, thereby enabling programmable entanglement operations.

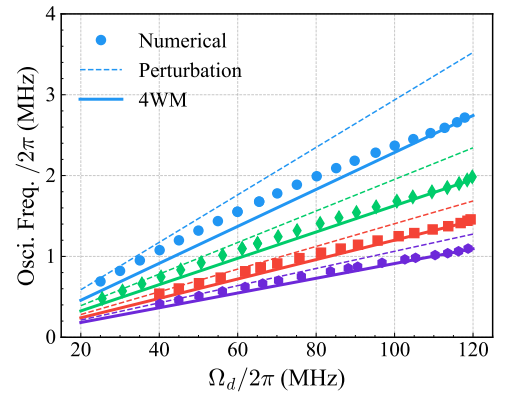


FIG. 7. Comparison of oscillation frequencies between perturbative predictions (dashed lines, Eq. (3)) and results derived from the four-wave mixing process (solid lines, Eq. (A8)).

Appendix B: Details of the Evolution Operator Simulation

In the non-interacting regime $g_{ij} = 0$, the system governed by Eq. (1) exhibits bare eigenstates $|ijk\rangle$, where $i, j, k \in \mathbb{N}$ label the individual transmon levels. When couplings are introduced, the eigenstates of H_0 evolve into dressed states $|\widetilde{ijk}\rangle$, characterized by slight energy shifts relative to their bare counterparts and a substantial overlap with the bare state. Each dressed eigenstate is labeled as $|\widetilde{ijk}\rangle$ according to the bare state with which it shares maximal overlap. The computational subspace is spanned by states $|\widetilde{ijk}\rangle$ with $i, j, k \in \{0, 1\}$.

To numerically construct the evolution operator, we simulate the time evolution of the system under Eq. (2) using QuTiP [63], initializing the dynamics with the computational states $|\psi_i\rangle$. The evolved states $|\psi'_i\rangle$ are projected onto the basis states to construct the operation matrix \tilde{U} , whose elements are given by $U_{ij} = \langle\psi_i|\psi'_j\rangle$. Note that \tilde{U} is not a unitary matrix in general due to leakage errors [28, 53, 59, 72]. From this procedure, we obtain the microwave-activated operation \tilde{U} and then implement a phase optimization protocol to derive the phase compensated unitary $U' = U_{\text{phase}}\tilde{U}(\phi)$. The performance of the implemented gate is quantified using the averaged gate fidelity metric [69],

$$F = \frac{|\text{Tr}(U_{\text{ideal}}^\dagger U')|^2 + \text{Tr}(U'^\dagger U')}{d(d+1)}, \quad (\text{B1})$$

where $d = 8$ represents the Hilbert space dimension of the three-qubit system, and U_{ideal} corresponds to the ideal gate defined in Eq. (6). The phase-compensated unitary U' is constructed as $U' = U_{\text{phase}}\tilde{U}(\phi)$, with ϕ denotes the pulse phase. Here, U_{phase} comprises three single-qubit virtual Z gates and two CPhases for AB and BC .

Appendix C: Details of Process Fidelity Simulations

We numerically simulate the system's time evolution by solving the Lindblad master equation (Eq. (2)) in QuTiP [63],

$$\dot{\hat{\rho}}(t) = -i[\hat{H}_{\text{RF}}(t), \hat{\rho}] + \sum_{\alpha} \left(\hat{L}_{\alpha} \hat{\rho} \hat{L}_{\alpha}^\dagger - \frac{1}{2} \{ \hat{L}_{\alpha}^\dagger \hat{L}_{\alpha}, \hat{\rho} \} \right), \quad (\text{C1})$$

where $\hat{\rho}$ is the density matrix, \hat{H}_{RF} represents the system Hamiltonian, and the Lindblad operators $\hat{L}_1 = \sqrt{\Gamma_1}|0\rangle\langle 1|$ (relaxation) and $\hat{L}_\phi = \sqrt{\Gamma_\phi/2}(|0\rangle\langle 0| - |1\rangle\langle 1|)$ (pure dephasing) model decoherence. As our gate protocol operates exclusively within the computational subspace, de-

coherence effects are restricted to transitions between $|0\rangle$ and $|1\rangle$ states.

To reconstruct the process matrix for the microwave-activated three-qubit gate, we prepare 64 initial states spanning the three-qubit Hilbert space: $\{|0\rangle, |1\rangle, (|0\rangle + |1\rangle)/\sqrt{2}, (|0\rangle - |1\rangle)/\sqrt{2}\}^{\otimes 3}$. These states evolve under \hat{H}_{RF} , with the pulse phase ϕ incorporated into the \hat{H}_{RF} in the simulation. The value of ϕ is directly derived from the average fidelity optimization protocol outlined in Sec. IV. The resulting density matrices ρ_{final} are corrected via the U_{phase} operation to mitigate static phase errors. The process matrix χ is reconstructed using the relation $\rho_{\text{final}} = \sum_{n,m} \chi_{nm} E_n \rho_{\text{ini}} E_m^\dagger$, where the basis operators E_n are selected from the Pauli tensor product set $\{I, \sigma_x, -i\sigma_y, \sigma_z\}^{\otimes 2}$ [73]. The process fidelity is calculated as $F_\chi = \text{Tr}(\chi' \chi_{\text{ideal}})$ [26, 74], with χ_{ideal} representing the ideal gate process matrix for U_{ideal} . The process matrix χ' integrates phase corrections implemented by U_{phase} , which operates on the final density matrix ρ_{final} through three single-qubit Z-rotations and two CPhase gates targeting qubit pairs AB and BC . The five phase parameters are further optimized using the phase values obtained from average fidelity optimization (Sec. IV) as initial conditions, with the process fidelity F_χ serving as the optimization target. Numerical results in Fig. 7 demonstrate gate performance under decoherence-free conditions. For large detuning $\Delta_{AB} = 0.877$ GHz, the process fidelity exceeds 98.5%, while increasing the detuning to $\Delta_{AB} = 0.977$ GHz further elevates fidelity beyond 99.0%. Notably, When incorporating experimentally realistic decoherence rates with relaxation and dephasing times $1/\Gamma_1 = 1/\Gamma_\phi = 100 \mu\text{s}$, the protocol can maintain a process fidelity exceeding 98.0%. The achieved fidelity demonstrates robust performance against relaxation and dephasing errors, validating the protocol's compatibility with realistic superconducting qubit platforms.

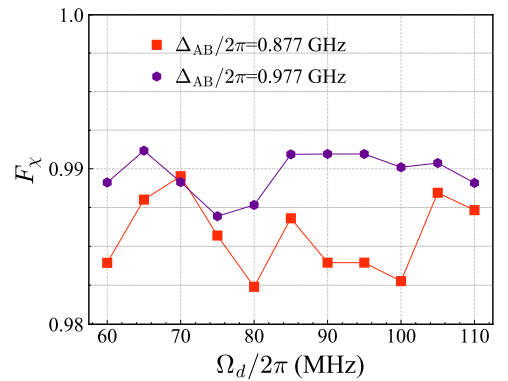


FIG. 8. The gate performance under decoherence-free conditions. The process fidelity exceeds 98.5% when the large detuning is $\Delta_{AB} = 0.877$ GHz, and upon increasing the detuning to $\Delta_{AB} = 0.977$ GHz, the fidelity is further elevated to exceed 99.0%.

-
- [1] S. Krinner, N. Lacroix, A. Remm, A. Di Paolo, E. Genois, C. Leroux, C. Hellings, S. Lazar, F. Swiadek, J. Herrmann, G. J. Norris, C. K. Andersen, M. Müller, A. Blais, C. Eichler, and A. Wallraff, Realizing repeated quantum error correction in a distance-three surface code, *Nature* **605**, 669 (2022).
- [2] Y. Zhao, Y. Ye, H.-L. Huang, Y. Zhang, D. Wu, H. Guan, Q. Zhu, Z. Wei, T. He, S. Cao, F. Chen, T.-H. Chung, H. Deng, D. Fan, M. Gong, C. Guo, S. Guo, L. Han, N. Li, S. Li, Y. Li, F. Liang, J. Lin, H. Qian, H. Rong, H. Su, L. Sun, S. Wang, Y. Wu, Y. Xu, C. Ying, J. Yu, C. Zha, K. Zhang, Y.-H. Huo, C.-Y. Lu, C.-Z. Peng, X. Zhu, and J.-W. Pan, Realization of an Error-Correcting Surface Code with Superconducting Qubits, *Phys. Rev. Lett.* **129**, 030501 (2022).
- [3] Z. Ni, S. Li, X. Deng, Y. Cai, L. Zhang, W. Wang, Z.-B. Yang, H. Yu, F. Yan, S. Liu, C.-L. Zou, L. Sun, S.-B. Zheng, Y. Xu, and D. Yu, Beating the break-even point with a discrete-variable-encoded logical qubit, *Nature* **616**, 56 (2023).
- [4] G. Q. AI and Collaborators., Quantum error correction below the surface code threshold, *Nature* **638**, 920 (2025).
- [5] J. Preskill, Quantum Computing in the NISQ era and beyond, *Quantum* **2**, 79 (2018).
- [6] K. Bharti, A. Cervera-Lierta, T. H. Kyaw, T. Haug, S. Alperin-Lea, A. Anand, M. Degroote, H. Heimonen, J. S. Kottmann, T. Menke, W.-K. Mok, S. Sim, L.-C. Kwek, and A. Aspuru-Guzik, Noisy intermediate-scale quantum algorithms, *Rev. Mod. Phys.* **94**, 015004 (2022).
- [7] B. Cheng, X.-H. Deng, X. Gu, Y. He, G. Hu, P. Huang, J. Li, B.-C. Lin, D. Lu, Y. Lu, C. Qiu, H. Wang, T. Xin, S. Yu, M.-H. Yung, J. Zeng, S. Zhang, Y. Zhong, X. Peng, F. Nori, and D. Yu, Noisy intermediate-scale quantum computers, *Front. Phys.* **18**, 21308 (2023).
- [8] C. Rigetti and M. Devoret, Fully microwave-tunable universal gates in superconducting qubits with linear couplings and fixed transition frequencies, *Phys. Rev. B* **81**, 134507 (2010).
- [9] J. M. Chow, A. D. Córcoles, J. M. Gambetta, C. Rigetti, B. R. Johnson, J. A. Smolin, J. R. Rozen, G. A. Keefe, M. B. Rothwell, M. B. Ketchen, and M. Steffen, Simple All-Microwave Entangling Gate for Fixed-Frequency Superconducting Qubits, *Phys. Rev. Lett.* **107**, 080502 (2011).
- [10] S. Sheldon, E. Magesan, J. M. Chow, and J. M. Gambetta, Procedure for systematically tuning up cross-talk in the cross-resonance gate, *Phys. Rev. A* **93**, 060302 (2016).
- [11] A. Patterson, J. Rahamim, T. Tsunoda, P. Spring, S. Jebari, K. Ratter, M. Mergenthaler, G. Tancredi, B. Vlastakis, M. Esposito, and P. Leek, Calibration of a Cross-Resonance Two-Qubit Gate Between Directly Coupled Transmons, *Phys. Rev. Appl.* **12**, 064013 (2019).
- [12] K. Heya and N. Kanazawa, Cross-cross resonance gate, *PRX Quantum* **2**, 040336 (2021).
- [13] A. Kandala, K. X. Wei, S. Srinivasan, E. Magesan, S. Carnevale, G. A. Keefe, D. Klaus, O. Dial, and D. C. McKay, Demonstration of a High-Fidelity cnot Gate for Fixed-Frequency Transmons with Engineered ZZ Suppression, *Phys. Rev. Lett.* **127**, 130501 (2021).
- [14] B. K. Mitchell, R. K. Naik, A. Morvan, A. Hashim, J. M. Kreikebaum, B. Marinelli, W. Lavrijsen, K. Nowrouzi, D. I. Santiago, and I. Siddiqi, Hardware-Efficient Microwave-Activated Tunable Coupling between Superconducting Qubits, *Phys. Rev. Lett.* **127**, 200502 (2021).
- [15] K. X. Wei, E. Magesan, I. Lauer, S. Srinivasan, D. F. Bogorin, S. Carnevale, G. A. Keefe, Y. Kim, D. Klaus, W. Landers, N. Sundaresan, C. Wang, E. J. Zhang, M. Steffen, O. E. Dial, D. C. McKay, and A. Kandala, Hamiltonian Engineering with Multicolor Drives for Fast Entangling Gates and Quantum Crosstalk Cancellation, *Phys. Rev. Lett.* **129**, 060501 (2022).
- [16] X.-L. Li, Z. Tao, K. Yi, K. Luo, L. Zhang, Y. Zhou, S. Liu, T. Yan, Y. Chen, and D. Yu, Hardware-efficient and fast three-qubit gate in superconducting quantum circuits, *Front. Phys.* **19**, 51205 (2024).
- [17] K. X. Wei, I. Lauer, E. Pritchett, W. Shanks, D. C. McKay, and A. Javadi-Abhari, Native two-qubit gates in fixed-coupling, fixed-frequency transmons beyond cross-resonance interaction, *PRX Quantum* **5**, 020338 (2024).
- [18] N. H. Le, M. Cykiert, and E. Ginossar, Scalable and robust quantum computing on qubit arrays with fixed coupling, *npj Quantum Inf.* **9**, 1 (2023).
- [19] J. M. Martinis and M. R. Geller, Fast adiabatic qubit gates using only σ_z control, *Phys. Rev. A* **90**, 022307 (2014).
- [20] M. Malekakhlagh, E. Magesan, and D. C. McKay, First-principles analysis of cross-resonance gate operation, *Phys. Rev. A* **102**, 042605 (2020).
- [21] F. Yan, P. Krantz, Y. Sung, M. Kjaergaard, D. L. Campbell, T. P. Orlando, S. Gustavsson, and W. D. Oliver, Tunable Coupling Scheme for Implementing High-Fidelity Two-Qubit Gates, *Phys. Rev. Appl.* **10**, 054062 (2018).
- [22] M. C. Collodo, J. Herrmann, N. Lacroix, C. K. Andersen, A. Remm, S. Lazar, J.-C. Besse, T. Walter, A. Wallraff, and C. Eichler, Implementation of Conditional Phase Gates Based on Tunable ZZ Interactions, *Phys. Rev. Lett.* **125**, 240502 (2020).
- [23] Y. Xu, J. Chu, J. Yuan, J. Qiu, Y. Zhou, L. Zhang, X. Tan, Y. Yu, S. Liu, J. Li, F. Yan, and D. Yu, High-Fidelity, High-Scalability Two-Qubit Gate Scheme for Superconducting Qubits, *Phys. Rev. Lett.* **125**, 240503 (2020).
- [24] M. A. Rol, F. Battistel, F. K. Malinowski, C. C. Bultink, B. M. Tarasinski, R. Vollmer, N. Haider, N. Muthusubramanian, A. Bruno, B. M. Terhal, and L. DiCarlo, Fast, High-Fidelity Conditional-Phase Gate Exploiting Leakage Interference in Weakly Anharmonic Superconducting Qubits, *Phys. Rev. Lett.* **123**, 120502 (2019).
- [25] V. Negirneac, H. Ali, N. Muthusubramanian, F. Battistel, R. Sagastizabal, M. S. Moreira, J. F. Marques, W. J. Vlothuizen, M. Beekman, C. Zachariadis, N. Haider, A. Bruno, and L. DiCarlo, High-Fidelity Controlled-Z Gate with Maximal Intermediate Leakage Operating at the Speed Limit in a Superconducting Quantum Processor, *Phys. Rev. Lett.* **126**, 220502 (2021).
- [26] Y. Sung, L. Ding, J. Braumüller, A. Vepsäläinen, B. Kannan, M. Kjaergaard, A. Greene, G. O. Samach, C. McNally, D. Kim, A. Melville, B. M. Niedzielski, M. E. Schwartz, J. L. Yoder, T. P. Orlando, S. Gustavsson,

- and W. D. Oliver, Realization of High-Fidelity CZ and ZZ-Free iSWAP Gates with a Tunable Coupler, *Phys. Rev. X* **11**, 021058 (2021).
- [27] F. Marxer, A. Vepsäläinen, S. W. Jolin, J. Tuorila, A. Landra, C. Ockeloen-Korppi, W. Liu, O. Ahonen, A. Auer, L. Belzane, V. Bergholm, C. F. Chan, K. W. Chan, T. Hiltunen, J. Hotari, E. Hyyppä, J. Ikonen, D. Janzso, M. Koistinen, J. Kotilahti, T. Li, J. Luus, M. Papic, M. Partanen, J. Rabinä, J. Rosti, M. Savvitskiy, M. Seppälä, V. Sevriuk, E. Takala, B. Tarasinski, M. J. Thapa, F. Tosto, N. Vorobeve, L. Yu, K. Y. Tan, J. Hassel, M. Möttönen, and J. Heinsoo, Long-distance transmon coupler with cz-gate fidelity above 99.8 %, *PRX Quantum* **4**, 010314 (2023).
- [28] H. Goto, Double-Transmon Coupler: Fast Two-Qubit Gate with No Residual Coupling for Highly Detuned Superconducting Qubits, *Phys. Rev. Appl.* **18**, 034038 (2022).
- [29] P. Zhao, D. Lan, P. Xu, G. Xue, M. Blank, X. Tan, H. Yu, and Y. Yu, Suppression of Static ZZ Interaction in an All-Transmon Quantum Processor, *Phys. Rev. Appl.* **16**, 024037 (2021).
- [30] R. Li, K. Kubo, Y. Ho, Z. Yan, Y. Nakamura, and H. Goto, Realization of High-Fidelity CZ Gate Based on a Double-Transmon Coupler, *Phys. Rev. X* **14**, 041050 (2024).
- [31] T.-M. Li, J.-C. Zhang, B.-J. Chen, K. Huang, H.-T. Liu, Y.-X. Xiao, C.-L. Deng, G.-H. Liang, C.-T. Chen, Y. Liu, H. Li, Z.-T. Bao, K. Zhao, Y. Xu, L. Li, Y. He, Z.-H. Liu, Y.-H. Yu, S.-Y. Zhou, Y.-J. Liu, X. Song, D. Zheng, Z. Xiang, Y.-H. Shi, K. Xu, and H. Fan, High-precision pulse calibration of tunable couplers for high-fidelity two-qubit gates in superconducting quantum processors, *Phys. Rev. Appl.* **23**, 024059 (2025).
- [32] J. Koch, T. M. Yu, J. Gambetta, A. A. Houck, D. I. Schuster, J. Majer, A. Blais, M. H. Devoret, S. M. Girvin, and R. J. Schoelkopf, Charge-insensitive qubit design derived from the Cooper pair box, *Phys. Rev. A* **76**, 042319 (2007).
- [33] J. M. Chow, J. M. Gambetta, A. D. Córcoles, S. T. Merkel, J. A. Smolin, C. Rigetti, S. Poletto, G. A. Keefe, M. B. Rothwell, J. R. Rozen, M. B. Ketchen, and M. Steffen, Universal Quantum Gate Set Approaching Fault-Tolerant Thresholds with Superconducting Qubits, *Phys. Rev. Lett.* **109**, 060501 (2012).
- [34] A. Morvan, L. Chen, J. M. Larson, D. I. Santiago, and I. Siddiqi, Optimizing frequency allocation for fixed-frequency superconducting quantum processors, *Phys. Rev. Res.* **4**, 023079 (2022).
- [35] S. Krinner, P. Kurpiers, B. Royer, P. Magnard, I. Tsitsilin, J.-C. Besse, A. Remm, A. Blais, and A. Wallraff, Demonstration of an All-Microwave Controlled-Phase Gate between Far-Detuned Qubits, *Phys. Rev. Appl.* **14**, 044039 (2020).
- [36] P. W. Shor, Scheme for reducing decoherence in quantum computer memory, *Phys. Rev. A* **52**, R2493 (1995).
- [37] D. Poulin, A. Kitaev, D. S. Steiger, M. B. Hastings, and M. Troyer, Quantum Algorithm for Spectral Measurement with a Lower Gate Count, *Phys. Rev. Lett.* **121**, 010501 (2018).
- [38] I. M. Georgescu, S. Ashhab, and F. Nori, Quantum simulation, *Rev. Mod. Phys.* **86**, 153 (2014).
- [39] D. G. Cory, M. D. Price, W. Maas, E. Knill, R. Laflamme, W. H. Zurek, T. F. Havel, and S. S. Somaroo, Experimental Quantum Error Correction, *Phys. Rev. Lett.* **81**, 2152 (1998).
- [40] P. Schindler, J. T. Barreiro, T. Monz, V. Nebendahl, D. Nigg, M. Chwalla, M. Hennrich, and R. Blatt, Experimental repetitive quantum error correction, *Science* **332**, 1059 (2011).
- [41] E. Dennis, Toward fault-tolerant quantum computation without concatenation, *Phys. Rev. A* **63**, 052314 (2001).
- [42] A. Paetznick and B. W. Reichardt, Universal Fault-Tolerant Quantum Computation with Only Transversal Gates and Error Correction, *Phys. Rev. Lett.* **111**, 090505 (2013).
- [43] N. Yu, R. Duan, and M. Ying, Five two-qubit gates are necessary for implementing the Toffoli gate, *Phys. Rev. A* **88**, 010304 (2013).
- [44] Y. Kim, A. Morvan, L. B. Nguyen, R. K. Naik, C. Jnger, L. Chen, J. M. Kreikebaum, D. I. Santiago, and I. Siddiqi, High-fidelity three-qubit iToffoli gate for fixed-frequency superconducting qubits, *Nat. Phys.* **18**, 783 (2022).
- [45] A. J. Baker, G. B. P. Huber, N. J. Glaser, F. Roy, I. Tsitsilin, S. Filipp, and M. J. Hartmann, Single shot i-Toffoli gate in dispersively coupled superconducting qubits, *Appl. Phys. Lett.* **120**, 054002 (2022).
- [46] A. Fedorov, L. Steffen, M. Baur, M. P. da Silva, and A. Wallraff, Implementation of a toffoli gate with superconducting circuits, *Nature* **481**, 170 (2012).
- [47] M. D. Reed, L. DiCarlo, S. E. Nigg, L. Sun, L. Frunzio, S. M. Girvin, and R. J. Schoelkopf, Realization of three-qubit quantum error correction with superconducting circuits, *Nature* **482**, 382 (2012).
- [48] L. B. Nguyen, Y. Kim, A. Hashim, N. Goss, B. Marinelli, B. Bhandari, D. Das, R. K. Naik, J. M. Kreikebaum, A. N. Jordan, D. I. Santiago, and I. Siddiqi, Programmable heisenberg interactions between floquet qubits, *Nat. Phys.* **20**, 240 (2024).
- [49] H.-T. Liu, B.-J. Chen, J.-C. Zhang, Y.-X. Xiao, T.-M. Li, K. Huang, Z. Wang, H. Li, K. Zhao, Y. Xu, C.-L. Deng, G.-H. Liang, Z.-H. Liu, S.-Y. Zhou, C.-P. Fang, X. Song, Z. Xiang, D. Zheng, Y.-H. Shi, K. Xu, and H. Fan, Direct implementation of high-fidelity three-qubit gates for superconducting processor with tunable couplers, *arXiv:2501.18319* (2025).
- [50] S. Li, J. Clark, S. Wang, Y. Wu, M. Gong, Z. Yan, H. Rong, H. Deng, C. Zha, C. Guo, L. Sun, C. Peng, X. Zhu, and J.-W. Pan, Realisation of high-fidelity nonadiabatic CZ gates with superconducting qubits, *npj Quantum Inf.* **5**, 84 (2019).
- [51] L. B. Nguyen, N. Goss, K. Siva, Y. Kim, E. Younis, B. Qing, A. Hashim, D. I. Santiago, and I. Siddiqi, Empowering a qudit-based quantum processor by traversing the dual bosonic ladder, *Nat. Commun.* **15**, 7117 (2024).
- [52] N. J. Glaser, F. Roy, and S. Filipp, Controlled-Controlled-Phase Gates for Superconducting Qubits Mediated by a Shared Tunable Coupler, *Phys. Rev. Appl.* **19**, 044001 (2023).
- [53] I. A. Simakov, G. S. Mazhorin, I. N. Moskalenko, S. S. Seidov, and I. S. Besedin, High-fidelity transmon-coupler-activated CCZ gate on fluxonium qubits, *Phys. Rev. Appl.* **21**, 044035 (2024).
- [54] W. Feng and D.-w. Wang, Quantum fredkin gate based on synthetic three-body interactions in superconducting circuits, *Phys. Rev. A* **101**, 062312 (2020).
- [55] X. Gu, J. Fernández-Pendás, P. Vikstål, T. Abad, C. Warren, A. Bengtsson, G. Tancredi, V. Shumeiko,

- J. Bylander, G. Johansson, and A. F. Kockum, Fast multiqubit gates through simultaneous two-qubit gates, *PRX Quantum* **2**, 040348 (2021).
- [56] C. W. Warren, J. Fernández-Pendás, S. Ahmed, T. Abad, A. Bengtsson, J. Biznárová, K. Debnath, X. Gu, C. Križan, A. Osman, A. Fadavi Roudsari, P. Delsing, G. Johansson, A. Frisk Kockum, G. Tancredi, and J. Bylander, Extensive characterization and implementation of a family of three-qubit gates at the coherence limit, *npj Quantum Inf.* **9**, 44 (2023).
- [57] T. Itoko, M. Malekakhlagh, N. Kanazawa, and M. Takita, Three-qubit parity gate via simultaneous cross-resonance drives, *Phys. Rev. Appl.* **21**, 034018 (2024).
- [58] M. Mariani, H. Wang, T. Yamamoto, M. Neeley, R. C. Bialczak, Y. Chen, M. Lenander, E. Lucero, A. D. O’Connell, D. Sank, M. Weides, J. Wenner, Y. Yin, J. Zhao, A. N. Korotkov, A. N. Cleland, and J. M. Martinis, Implementing the quantum von Neumann architecture with superconducting circuits, *Science* **334**, 61 (2011).
- [59] E. Barnes, C. Arenz, A. Pitchford, and S. E. Economou, Fast microwave-driven three-qubit gates for cavity-coupled superconducting qubits, *Phys. Rev. B* **96**, 024504 (2017).
- [60] S. Shirai, Y. Okubo, K. Matsuura, A. Osada, Y. Nakamura, and A. Noguchi, All-Microwave Manipulation of Superconducting Qubits with a Fixed-Frequency Transmon Coupler, *Phys. Rev. Lett.* **130**, 260601 (2023).
- [61] R. Lescanne, S. Deléglise, E. Albertinale, U. Réglade, T. Capelle, E. Ivanov, T. Jacqmin, Z. Leghtas, and E. Flurin, Irreversible qubit-photon coupling for the detection of itinerant microwave photons, *Phys. Rev. X* **10**, 021038 (2020).
- [62] Z. Leghtas, S. Touzard, I. M. Pop, A. Kou, B. Vlastakis, A. Petrenko, K. M. Sliwa, A. Narla, S. Shankar, M. J. Hatridge, M. Reagor, L. Frunzio, R. J. Schoelkopf, M. Mirrahimi, and M. H. Devoret, Confining the state of light to a quantum manifold by engineered two-photon loss, *Science* **347**, 853 (2015).
- [63] J. Johansson, P. Nation, and F. Nori, Qutip: An open-source python framework for the dynamics of open quantum systems, *Comput. Phys. Commun.* **183**, 1760 (2012).
- [64] F. Motzoi, J. M. Gambetta, P. Rebentrost, and F. K. Wilhelm, Simple Pulses for Elimination of Leakage in Weakly Nonlinear Qubits, *Phys. Rev. Lett.* **103**, 110501 (2009).
- [65] J. M. Gambetta, F. Motzoi, S. T. Merkel, and F. K. Wilhelm, Analytic control methods for high-fidelity unitary operations in a weakly nonlinear oscillator, *Phys. Rev. A* **83**, 012308 (2011).
- [66] R. Schutjens, F. A. Dagga, D. J. Egger, and F. K. Wilhelm, Single-qubit gates in frequency-crowded transmon systems, *Phys. Rev. A* **88**, 052330 (2013).
- [67] N. Sundaresan, I. Lauer, E. Pritchett, E. Magesan, P. Jurcevic, and J. M. Gambetta, Reducing unitary and spectator errors in cross resonance with optimized rotary echoes, *PRX Quantum* **1**, 020318 (2020).
- [68] S. E. Economou, High-fidelity quantum gates via analytically solvable pulses, *Phys. Rev. B* **85**, 241401 (2012).
- [69] L. H. Pedersen, N. M. Møller, and K. Mølmer, Fidelity of quantum operations, *Phys. Lett. A* **367**, 47 (2007).
- [70] J. Chu and F. Yan, Coupler-Assisted Controlled-Phase Gate with Enhanced Adiabaticity, *Phys. Rev. Appl.* **16**, 054020 (2021).
- [71] P. Zhao, X. Tan, H. Yu, S.-L. Zhu, and Y. Yu, Simultaneously exciting two atoms with photon-mediated Raman interactions, *Phys. Rev. A* **95**, 063848 (2017).
- [72] P. Xu, Q. Jing, P. Zhao, and Y. Yu, Microwave-driven *iswap*-like gate for fixed-frequency superconducting transmon qubits, *Phys. Rev. A* **108**, 032615 (2023).
- [73] C.-T. Chen, Y.-H. Shi, Z. Xiang, Z.-A. Wang, T.-M. Li, H.-Y. Sun, T.-S. He, X. Song, S. Zhao, D. Zheng, K. Xu, and H. Fan, ScQ cloud quantum computation for generating Greenberger-Horne-Zeilinger states of up to 10 qubits, *Sci. China. Phys. Mech. Astron.* **65**, 110362 (2022).
- [74] L. B. Nguyen, G. Koolstra, Y. Kim, A. Morvan, T. Chistolini, S. Singh, K. N. Nesterov, C. Jünger, L. Chen, Z. Pedramrazi, B. K. Mitchell, J. M. Kreikebaum, S. Puri, D. I. Santiago, and I. Siddiqi, Blueprint for a high-performance fluxonium quantum processor, *PRX Quantum* **3**, 037001 (2022).